Scientific Research Publishing

Advances in Nanoparticles, 2023, 12, 106-122
https://www.scirp.org/journal/anp
ISSN Online: 2169-0529
ISSN Print: 2169-0510

Synthesis, Characterization, and Effects of Morphology on the Magnetic Application Base Properties of Pure Nickel Oxide (NiO) and Cobalt-Doped Nickel Oxide/Nickel Hydroxide ($Co_xNi_{1-x}O/Ni(OH)_2$) Nanocomposites

Ekane Peter Etape[1*], Oga Eugene Agbor[1], Beckley Victorine Namondo[1], Zoubir Benmaamar[2], Josepha Foba-Tendo[1], John Ngolui Lambi[3]

[1]Department of Chemistry, Faculty of Science, University of Buea, Buea, Cameroon
[2]Department of Chemistry, Saad Dahlab University, Blida, Algeria
[3]ENS, Yaoundé, University of Yaoundé I, Yaounde, Cameroon
Email: *ekane20022001@yahoo.fr

How to cite this paper: Etape, E.P., Agbor, O.E., Namondo, B.V., Benmaamar, Z., Foba-Tendo, J. and Lambi, J.N. (2023) Synthesis, Characterization, and Effects of Morphology on the Magnetic Application Base Properties of Pure Nickel Oxide (NiO) and Cobalt-Doped Nickel Oxide/Nickel Hydroxide ($Co_xNi_{1-x}O/Ni(OH)_2$) Nanocomposites. *Advances in Nanoparticles*, **12**, 106-122.
https://doi.org/10.4236/anp.2023.123009

Received: May 25, 2023
Accepted: July 17, 2023
Published: July 20, 2023

Abstract

Nano particle (NP) morphology is one of the material properties at the origin of potential application base properties exploited in several engineering and technology domains, such as fuel cell, electrodes, catalysis, sensing, electric, thermal, magnetic, and photovoltaic applications. The general properties and particle morphology of nickel oxide/Nickel hydroxide NPs can be modified by the introduction of impurity atoms or ions. Nano sized nickel oxide/nickel hydroxide nanocomposites were obtained from the thermal decomposition of single molecular precursors synthesized by a modified oxalate route using Carambola fruit juice as a precipitating agent. The compositional and morphological variations were studied by introducing cobalt as an impurity ion at different w/w% fractions (0%, 0.1%, 0.3%, 0.5%, 1%, 3%, 5.0%, 40.0% and 50.0%) into the microstructure of the nickel oxide/hydroxide. The precursors were characterized by FT-IR, while TGA/DTG analysis was carried out to decompose the precursors. The precursors decomposed at 400˚C and were characterized by PXRD and SEM/TEM. The results revealed that Pure Nickel Oxide (NiO) and, Cobalt-doped Nickel Oxide/nickel hydroxide ($Co_xNi_{1-x}O/Ni(OH)_2$) Nano composites have been synthesized and the synthesized samples have exhibited three distinct morphologies (porous face-centered cubic nano rods, rough and discontinuous $Co_xNi_{1-x}O/Ni(OH)_2$) composite and, smooth and continuous mix spherical/cuboidal mixed morphological phase of (NiO/CoO). The morphology of the NPs varied with the introduction of

the dopant atoms and with increase in the concentration of dopant atoms in the composite. Magnetic studies using vibrating sample magnetometry revealed superparamagnetic properties which correlated strongly with particle size, shape and morphology. Observed values of retention (4.50×10^{-3} emu/g) and coercivity (65.321 Oe) were found for 0.5 w/w% corresponding to impregnated porous nanorods of Co-doped NiO, and retention (9.03×10^{-3} emu/g) and coercivity (64.341 Oe), for X = 50.0%, corresponding to an aggregate network of a Nano spherical/cubic CoO/NiO mixed phase. Magnetic properties within this range are known to improve the magnetic memory and hardness of the magnetic materials. Therefore, the synthesized Cobalt-doped Nickel Oxide/nickel hydroxide ($Co_xNi_{1-x}O/Ni(OH)_2$) Nano composites have potential applications in Magnetic memories and hardness of magnetic materials.

Keywords

Nickel Oxide/Hydroxide, Doping, Morphology, Magnetic Properties, Carambola Fruit Juice

1. Introduction

The nanoparticle size effect in technological evolution has manifested advantages in physical, chemical, and biological application base properties. Nickel oxide is a perovskite material whose size effect and morphology of nanoparticles have attracted much attention due to the strong correlation between properties, size and morphology. The nickel oxide nanoparticle is a p-type semiconductors with a band gap ranging from 3.1 to 4.0 eV, which has exhibited increased chemical stability, electrocatalytic properties, super conductance and electron transfer capability. Nano particle morphology is at the origin of potential application base properties exploited in several engineering and technology domains, such as photovoltaic [1], Solar cells [2], Catalysis [3], Magnetic [4], Electric [5], sensing [6] and energy storage [7] applications. The general properties and particle morphology of nickel oxide NPs can be modified by the introduction of impurity atoms or ions by doping. Several wet chemical methods have been successfully employed for the synthesis of nanoparticles, but the oxalate route has singled itself out by showing control over the nanoparticle (NP) morphology. The oxalate route has the metal oxalate as a single molecular precursor with carboxylate groups acting as chelating ligands between metal atoms and the resultant highly regular 3D structures generally called metal-organic frameworks (MOFs). The oxalate route takes advantage of the fact that the precursor thermally decomposed under mild thermal conditions producing CO_2/CO gas mixtures and either pure metal and/or metal oxide depending on the environmental conditions (oxidizing; air or oxygen), neutral (nitrogen, helium) or reducing (hydrogen) [8]. The Carambola fruit juice method is a modified oxalate method which uses

naturally occurring dissolved oxalate in the fruit sap. This natural juice rich in oxalate mitigates the solubility problems of commercial oxalates. The juice is ecofriendly, cheap and contains a consequent renewable source of oxalate. Many research efforts have been devoted to thermal decomposition studies of nickel oxalate. In a previous study, Nguimezong *et al.* [9] and in conformity with other literature demonstrated that the thermal decomposition of nickel oxalate dihydrate proceeded via two main stages; dehydration and decomposition but the characteristics of these stages are greatly influenced by many factors, such as the heating rate, and mass of the sample [10] and, the temperature of preparation and catalysts [11]. The thermal decomposition of nickel oxide in air has been broadly studied [12] [13] [14], and in all these studies, the decomposition stage was observed to be exothermic with the final product found to be essentially NiO under oxidizing conditions (air, O_2). In addition, decomposition in air occurs at a lower temperature. Thermogravimetric analysis (TGA) and differential thermal analysis (DTA) are the most available techniques used for studying the process of dehydration/decomposition of metal oxalates. These thermal analyses have been coupled with mass spectrometry (MS), gas-liquid chromatography, and Fourier transform infrared spectroscopy to monitor evolving gases. Nickel oxide has been co-doped with various transition metals to modify its morphology and stability. The effects of Co, Cu, and Zn dopants on the optical, morphological, electrochemical, and electrochromic properties of NiO thin films prepared via sol-gel spin coating have been reported, and the NiO thin films were composed of nanoparticles and exhibited increased surface coverage compared with the undoped sample [15]. By incorporating Co, Cu, and Zn dopants, the Co-doped NiO sample demonstrated excellent long-term electrochemical stability, retaining a capacity of ~88% after 2000 cycles, representing a notable improvement compared with the values of ~70%, ~56%, and ~56% recorded for undoped, Cu-, and Zn-doped NiO, respectively [15]. Copper-doped nickel oxide has been evaluated for hybrid nano lubricants as a compressor oil, and the results showed that doping increased the coefficient of performance (COP) value by 18.45% [16]. The effect of cobalt doping on the electrochemical properties of sprayed nickel oxide thin films was reported in the literature [17], and Co doping of nickel oxide led to a significant enhancement in the electrochemical properties of the NiO electrode material, which is a suitable alternate electrode material for supercapacitor applications. Highly porous Co-doped NiO nanorods with a high specific surface area and abundant nanopores have been synthesized by the oxalate route, and the products showed a significant increase in catalytic activity for the oxygen evolution reaction (OER), which was attributed to a combination of a highly porous NiO nanoarchitecture and the effect of the Co dopant [18]. In an investigation on the suitability of Co-doped NiO_x nanoparticles as HTMs, nanoparticles containing different concentrations (0 - 5 mol%) of Co ions were synthesized, and they demonstrated a double effect of Co doping. On the one hand, Co doping arises from surface recombination while on

the other hand, Co doping influences the properties of the perovskite grown on top of the Co-NiO_x substrates, improving the morphology as a consequence of grain size enlargement and reducing bulk recombination [19]. We think that impregnating NiO with OH may reveal even more interesting morphological changes which will infer on the magnetic properties of the new materials. In this study, nano sized nickel oxide/hydroxide composites were obtained from the thermal decomposition of a single molecular precursor synthesized by a modified oxalate route using Carambola fruit juice as a precipitating agent. The compositional and morphological variations were modified by introducing cobalt as an impurity ion at different w/w % fractions of cobalt (0, 0.1, 0.3, 0.5, 3, 4.0 and 5.0) into the microstructure of the nickel oxide NPs.

2. Materials and Methods

2.1. Materials

Cobalt (II) chloride and nickel (II) chloride were obtained from Sigma Aldrich with 97% purity, while the fruit juice for precipitation was obtained from Ripe Carambola fruits. The juice was prepared as reported in the literature [9] [20] and kept in a freezer until further use.

2.2. Methods

2.2.1. Synthesis Protocol

Co_x-$Ni_{1-x}O$ NPs were synthesized by a co-precipitation procedure (x = 0, 0.1, 0.3, 0.5, 3, 5, 40.0 and 50.0). One hundred milliliters of the juice extract were poured into a 250 mL round bottom flask and immersed into a water bath maintained at 80˚C. The appropriate metal ion solutions [(1 − x) + x] 100 mL were added slowly into the juice while stirring for 2 hrs. The mixtures were allowed to cool to room temperature and the precipitates obtained, filtered and washed three times with distilled water followed by ethanol and then dried in a glass oven at 80˚C for 2 h. The dried samples (Precursors) obtained were preserved for analysis.

2.2.2. Characterization Techniques

FTIR spectra of the samples were recorded on a PerkinElmer Spectrum Two Universal Attenuated Total Reflectance Fourier Transform Infrared (UATR-FTIR) spectrometer in the range of 390 - 4200 cm^{-1}. Thermogravimetric analysis (TGA) was obtained using a Pyris 6 PerkinElmer TGA 4000 thermal analyzer. The thermal studies to determine the right annealing temperature were conducted between 30˚C and 900˚C in air at a flow rate of 20 mL/min and a temperature ramp of 10˚C/min. To identify the structure and phase purity of the prepared sample, powder X-ray diffraction (XRD) analysis was performed on a Philips PW-1710 diffractometer with CuKα radiation (λ = 1·540598 Å) at room temperature. The surface morphology of the prepared sample was determined by scanning electron microscopy (SEM, Philips XL-20) and low magnification TEM, while the magnetization measurement (M-H characteristics) of the sample was

recorded using a vibrating sample magnetometer (VSM) where the magnetic field could be varied up to 1·8 Tesla.

3. Results and Discussion

3.1. Characterization of the Samples

3.1.1. Thermogravimetric/Differential Thermogravimetric Analysis (TGA/DTG)

Thermal studies by TGA/DTG analysis revealed the decomposition profile of the precursors and suggested the decomposition temperature of the samples. **Figure 1(a)** shows the TGA/DTG profiles of the precursors as consisting of two stages, notably dehydration and decomposition, while the EDS reveals that nickel was the metal ion present in the final decomposition product. The dehydration stage occurring at 108˚C ± 2˚C is accompanied by a mass loss of 17.4% ± 0.4% relative to 19.718% theoretically expected. The difference of 2.318% is attributed to the existence of dehydrated and hydrated nickel oxalate [21] [22] or adsorbed water molecules in the pores of the dehydrated nickel oxalate crystallites [23]. The decomposition stage which occurred at 380˚C ± 8˚C and accompanied by a mass loss of 29.27%, which compares well with the theoretically calculated value (29.372%). However, the difference in water of hydration now liberated at the decomposition stage revealed a net mass of 2.42% attributed to some molecules of hydroxide $Ni(OH)_2$ in the pores of the nickel oxide crystallites formed or just adsorbed on the nickel oxide surface by chemisorption. This observation was confirmed by the EDS of the decomposed samples integrated in **Figure 1(a)**. However, annealing at a higher temperature (600˚C), leads to the decomposition of the relatively stable hydroxide intermediate to pure NiO nanoparticles. The relatively stable intermediate also decomposed when annealing at 400˚C is prolonged to 6hrs. These results suggested that the total decomposition of the reaction intermediate required prolonged heating (calcinations for a longer period). It is interesting to note that the samples exhibited the same thermal decomposition profile, as shown in **Figure 1(a)** and **Figure 1(b)**. The observation is attributed to the closeness of the chemistry of nickel oxide to that of cobalt oxide (CoO and Co_3O_4), as observed from their heat of formations −57.3 ± 0.1 and −57.1 ± 0.3 kcal/mol. for NiO and CoO, respectively (Boyle B. J., 1954) [24]. It is by this advantage that the nanocomposite $Ni_{1-x}Co_xO/Ni(OH)_2$ is obtained by decomposing the precursor at 400˚C for 3 hrs.

3.1.2. Fourier Transform Infrared Spectroscopy (FTIR) Analysis

The FTIR profiles for the pure and Co-doped nickel oxalate (precursors) are presented in **Figure 2**. The principal FTIR characteristic absorption bands of samples x = 0.0%, 0.1%, 0.3%, 3.0% and 5.0% and their assignments are summarized in **Table 1**. The profiles of the samples in the series of precursors and decomposed products are similar within each series but differ between the series, indicating that new bonding modes existed in the products. However, within each series, slight shifts were revealed as the doping fractions increased. The shift

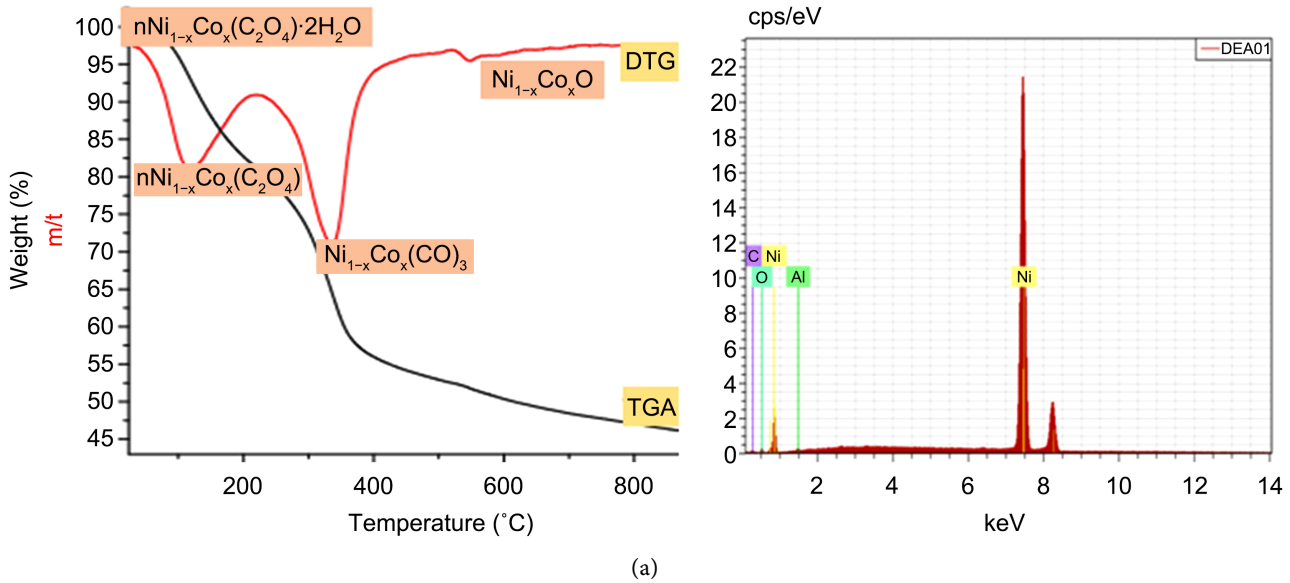

(a)

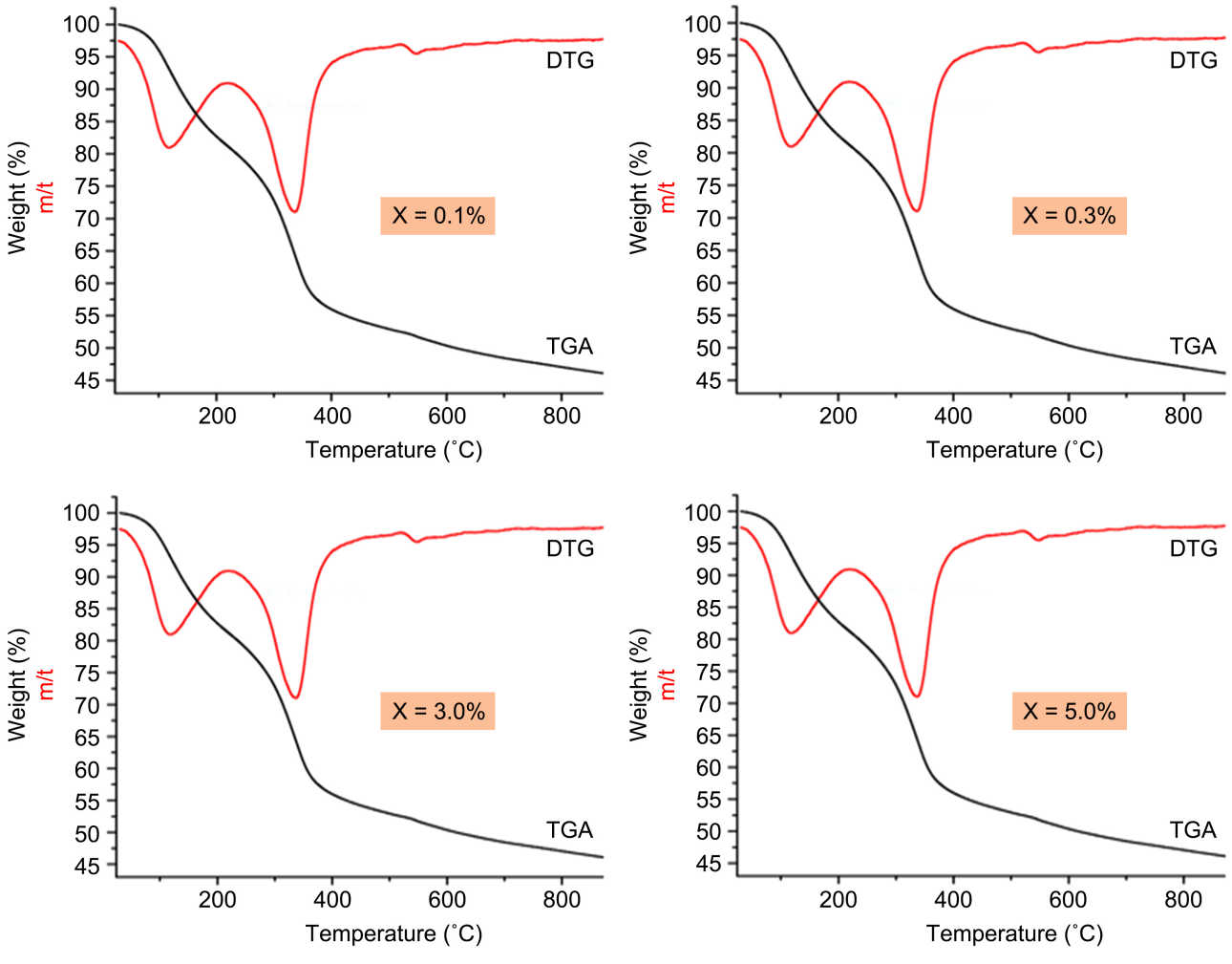

(b)

Figure 1. (a) Decomposition profiles (TGA/DTG) of the as-synthesized precursors x = 0.0%, and EDS, showing the metal ions present in decomposed samples; (b) decomposition profiles (TGA/DTG) of the as-synthesized precursors (x = 0.1%, 0.3%, 3.0%, and 5.0%).

is attributed to the presence of cobalt ions in the microstructure of NiO, and the insignificance in variability between the profiles after doping could be attributed to the closeness of the bonding properties between nickel and cobalt. In the decomposed products and for all doping fractions, two absorption bands were observed at 542 cm^{-1} and 358 cm^{-1} corresponding to the metal-oxygen bonds (Ni-O and Co-O, respectively), which were in agreement with the expected results. The absence of the free carbonyl [ν(C=O)] vibration expected at approximately 1700 cm^{-1} is an indication that the carboxylate group is completely involved in the coordination. The bonding mode of oxalate is determined by calculating the separation between the bands, $\Delta\nu$ (= νCOOasym − νCOOsym), which presented $\Delta\nu$ between 140 cm^{-1} and 200 cm^{-1} suggesting that the bonding mode of the oxalate ions with the metal atoms is the bridged bidentate mode [25]. Our results showed that $\Delta\nu$ was 150 cm^{-1}, corresponding to the bridged bidentate, which indicated.

Table 1. FTIR absorption bands of samples x = 0.0%, 0.1%, 0.3%, 3.0%, and 50.0%, and their assignments.

Functional groups	Kind of bonding	Wavenumber (cm^{-1})
O-H/H_2O	ϒ	3395, between 1610 and 1625 cm^{-1} [26]
	Δ	1536
O-H/Ni-OH	ϒ	3420
CH/CH_3	υ_{as}	2957
	υ_s	2872
CH/CH_2	υ_{as}	2923
	υ_s	2853
C-C	υ_{as}	920
OCO, ν(C-O + δ(O-C = O))	υ_{as}	1581
	υ_s	1313 - 1320 cm^{-1} and 825 - 826 cm^{-1} [20]
	Δ	674
	Π	641
$(CH_2)_6$	Δ	1320
	P	743
Ni-O	ϒ	591, 530 and 481 cm^{-1} were assigned to: V(O-Ni-O), V(Ni-O) + V(C-C) and V(Ni-O), respectively [17] [27].
Co-O	ϒ	370

υ: stretching (as: asymmetric; s: symmetric); δ: deformation in the plane; π: deformation outside the plane and ρ: wagging.

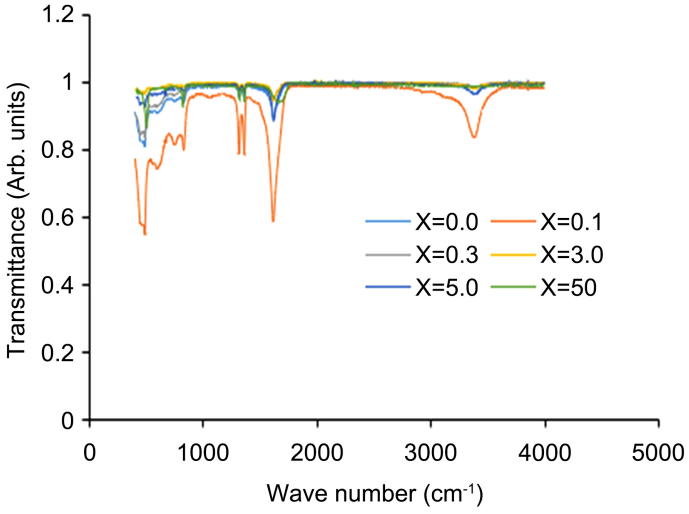

(a)

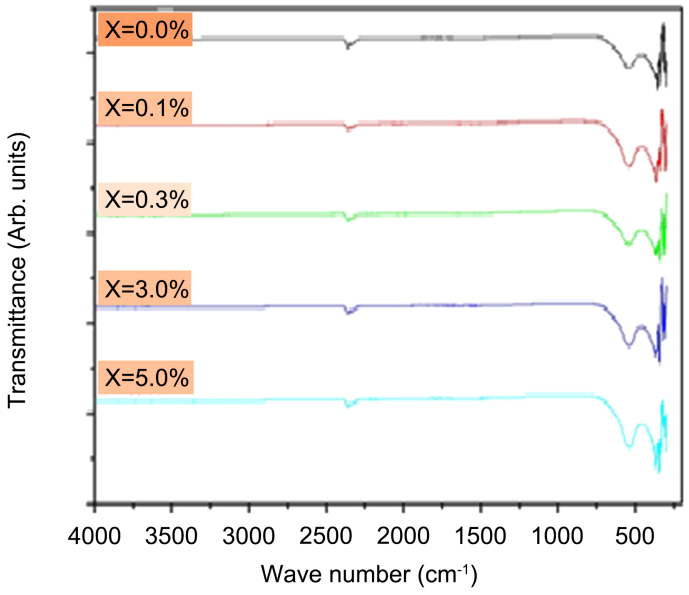

(b)

Figure 2. (a) FTIR spectra of the as-synthesized precursors; (b) FTIR spectra of the decomposed products.

3.1.3. Phase Identification

The powder X-ray diffractograms (PXRD) for the calcined products of the samples are shown in **Figure 3(a)** (sample calcined at 400˚C for 6 hrs.) and **Figure 3(b)** (samples calcined at 400˚C for 4 hrs.). Diffraction peaks identified from **Figure 3(a)** are at 2θ values of 37.70˚, 43.54˚, 61.84˚, and 74.65˚ indexed to the (111), (200), (220) and (311) crystal planes, which match with [JCPDS card No: 47-1049] of nickel oxide nanofibers. However, in **Figure 3(b)**, in addition to the peaks observed in **Figure 3(a)**, there is another peak at 2θ values of 51.64 indexed to the (112) crystal plane which matches with [JCPDS card no. 14-0481] of $Ni(OH)_2$. There were no other impurity peaks suggesting that the samples calcined at 400˚C for 3 hrs are made up of a mixed phase of NiO and $Ni(OH)_2$.

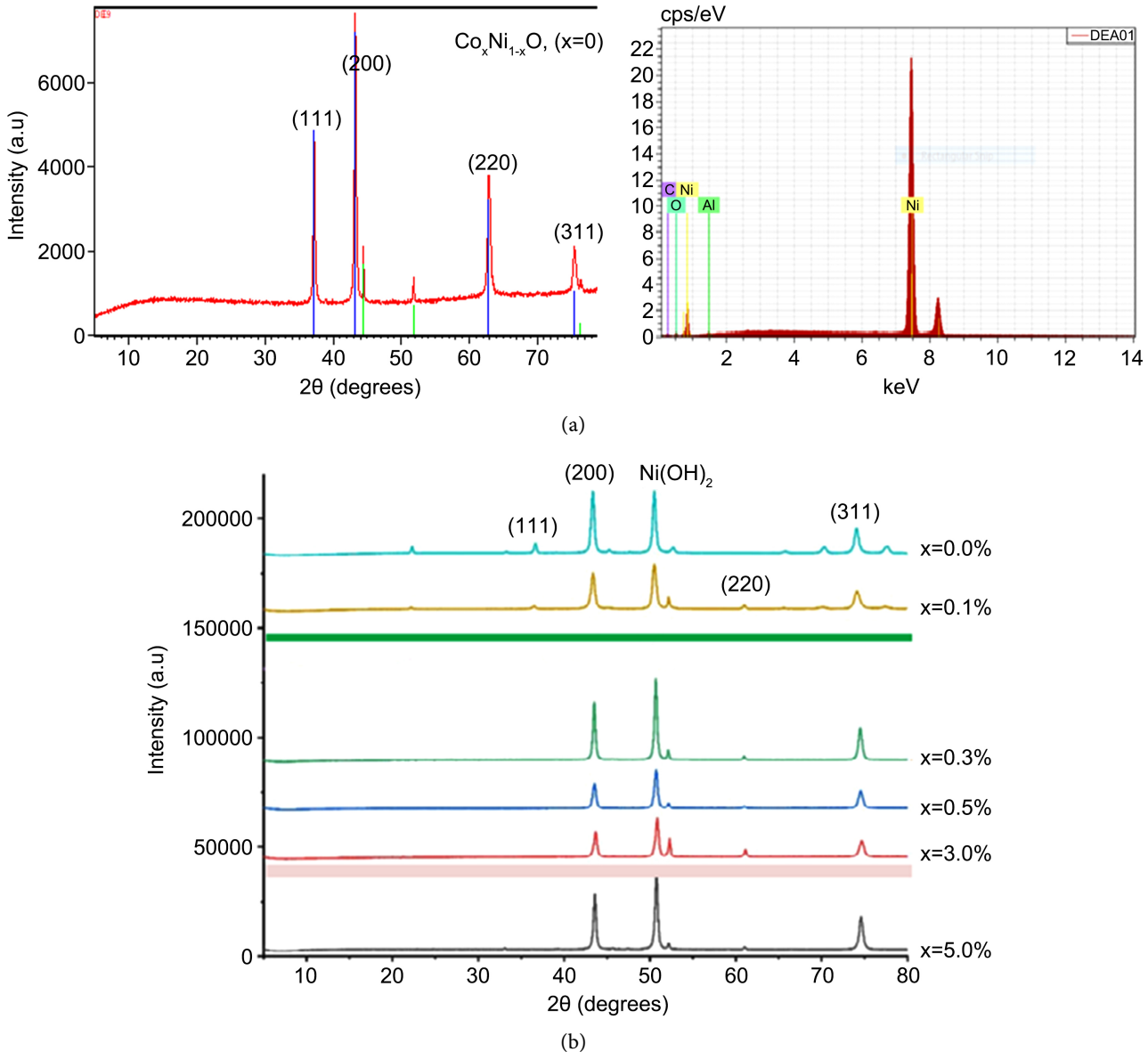

Figure 3. (a) X-ray/EDS of the as-synthesized composites (x = 0) calcined at 400˚C for 6 hrs; (b) PXRD of the as-synthesized composites (x = 0.0%, 0.1%, 0.3%, 0.5%, 3.0% and 5.0%) calcined at 400˚C for 3 hrs.

The absence of the peak at 2θ value of 45.34 in the X-ray diffractograms of the products indicated the absence of Ni metal in the decomposed sample. Although there are no metal oxide impurity peaks at low Co doping fractions, there are slight phase shifts in the XRD peak position of the crystal planes of the NiO phase towards higher angles as the doping fraction increased, which demonstrated the incorporation of Co impurity atoms in the host matrix. The substitution came with a little change in the Co/Ni atomic radius ratio (although there is a close similarity in the radius of Co(0.79 Å) and Ni(0.83 Å) atoms), which leads to the distortion in the crystallite microstructure of Nickel oxides and the eventual shifts in 2θ values. A separate evaluation of the individual X-ray diffractograms showed very little change in peak intensity, especially after 0.5% mol Co

doping, indicating very little variability in the crystallite sizes. However, the initial increase in intensity for doping fractions up to 0.3% mol Co-doping indicated an increase in the number of crystallites and similar observations were reported in the literature [28] [29] [30].

The crystalline sizes of the particles (pure and cobalt-doped NiO/$Ni(OH)_2$ nanoparticles) were determined using Debye Scherer's relation, Equation (1)

$$D = k\lambda/\beta\cos\theta \tag{1}$$

where D is the crystalline size, β is the full width half-maximum value of the high intensity peak, k is the shape factor (0.9), λ = wavelength of the radiation with value (λ) = 0.15406 nm, θ = Bragg's angle and β = full width at half maximum (FWHM) peak. Line broadening due to the instrument was subtracted from the peak width before calculating the crystallite size using Equation (2):

$$\beta^2 = \beta^2\text{meas} - \beta^2\text{equi} \tag{2}$$

where β means = measured full width at half maximum of peak β, equi = instrumental broadening Standard Silicon sample was used, whose β value was 0.09821 at $2\theta = 29^\circ$ with (hkl) values (200) for NiO and (112) for Ni_2O_3 profiles in **Figure 3**. The particle distancing was calculated using Bragg's equation (Equation (3)):

$$2d\sin\theta = n\lambda \tag{3}$$

For $n = 1$, and $\lambda = 0.154$ nm.

The crystallite sizes are found to decrease with increase in dopant concentrations and vary between 7.8 nm, 7.3 nm, and 7.1 nm for various identified diffraction peaks. These results compare with those reported in the literature [31].

3.1.4. Morphology: Scanning Electron Microscopy (SEM)/Low Magnification Transmission Electron Microscopy (TEM)

Figure 4 shows the scanning electron micrographs of the synthesized samples. Three different morphologies are observed as the concentration of the dopant increased. The predominant morphology is the porous nanorods, which are exhibited by five different test samples (x = 0.0, 0.1, 0.2, 0.3, 0.5).

A clearer view of the nano rod morphology is observed under TEM at low magnification (**Figure 4(b)**), where the nano rods are seen to be rough surfaced, made up of nano grains with distinct boundaries, regularly arranged and interspaced with pores. The nano rods measured about 1 μm in length and 100 nm in diameter. The presence of pores granted hydroxides molecules easy access. The dopants ions had three possibilities of reacting with the main matrix: to replace nickel atoms, fill the pores, or be adsorbed on the rough nano rod surfaces. At lower Co doping mol% fractions, such as 0.1 mol% and 0.3 mol%, the cobalt atoms are systematically substituted for Ni atoms in the nano rod microstructure, thereby modifying the surface area and the size of the nano rods while at relatively high dopant concentrations, such as 3%, both impregnation of the pores and adsorption of the Co atoms in the NiO matrix occur. As the doping progressed to very high concentrations of dopants (Co), such as 40% and 50%,

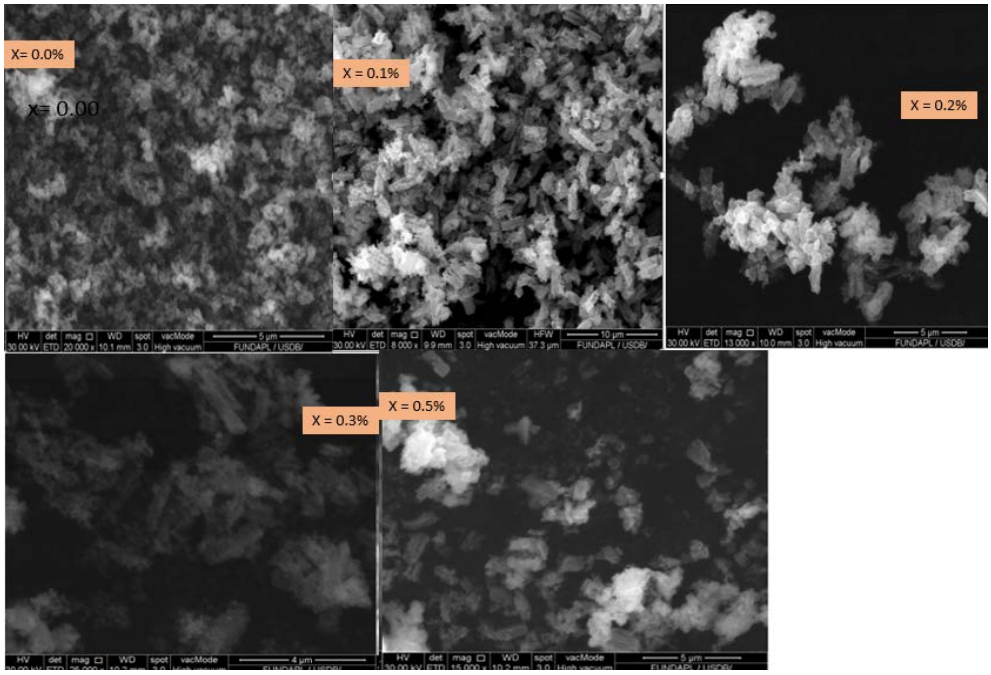

(a)

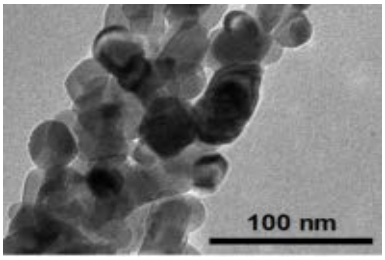

(b)

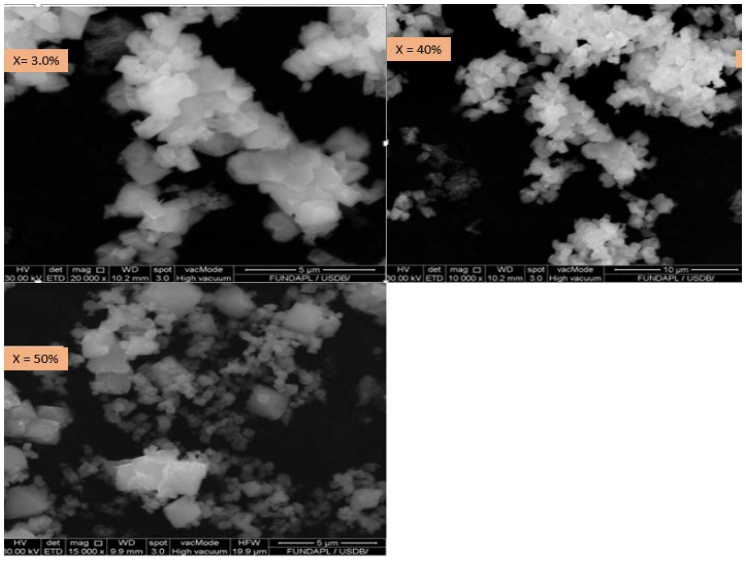

(c)

Figure 4. (a) SEM pictures of Ni1-xCoxO (x = 0.0%, 0.1%, 0.2%, 0.3%, and 0.5%); (b) low-magnification TEM image of a pure NiO nano rod (x = 0.0%); (c) SEM pictures of composites with high concentrations cobalt ions (x = 3.0%, 40.0%, and 50.0%).

the pores are further impregnated with the dopants leading to the disintegration of the nano rod framework into cuboidal and spherical grains, attributed to CoO and Nickel Oxide faces (Figure 4(c)). These grains agglomerated into porous aggregated clusters held together by strong attractive forces which interconnect the masses. The particle sizes observed from the TEM micrograph are in the range of 10 nm, which confirms the grain size calculation from the XRD results (between 7.0 - 7.8 nm).

3.2. Magnetic Studies: Vibrating Sample Magnetometry (VSM)

Five of the samples selected from three different morphologies (Porous nano rods, nano rods with filled/filling pores, and interconnect masses) were subjected to magnetic studies to evaluate the effects of dopant concentration and/or morphology of the products on the magnetic properties. The magnetic parameters of the pure products and Co-doped nanoparticles are presented in Table 2, while Figure 5 shows the magnetic characteristic curves of the samples analyzed using a vibrating sample magnetometer at room temperature. The magnetization curve for the synthesized magnetite nanocomposites all showed very small hysteresis behaviors and exhibit relatively very low remnant magnetization (0.00105 - 0.00903 emu/g). These suggest that the synthesized nano composites display super paramagnetic behavior at room temperature. The observation is attributed to the very small particle sizes (7.0 - 7.8 nm) of the paramagnetic synthesized Nanocomposites which are smaller than the critical size of the magnetic domain size (20 nm) [27]. Furthermore, the nanocomposites also show very low saturation magnetization (M_s) values compared to bulk. The saturated magnetization values of the nanocomposites obtained were in the range (0.0183 - 0.240 emu/g) suggesting the existence of paramagnetic behavior.

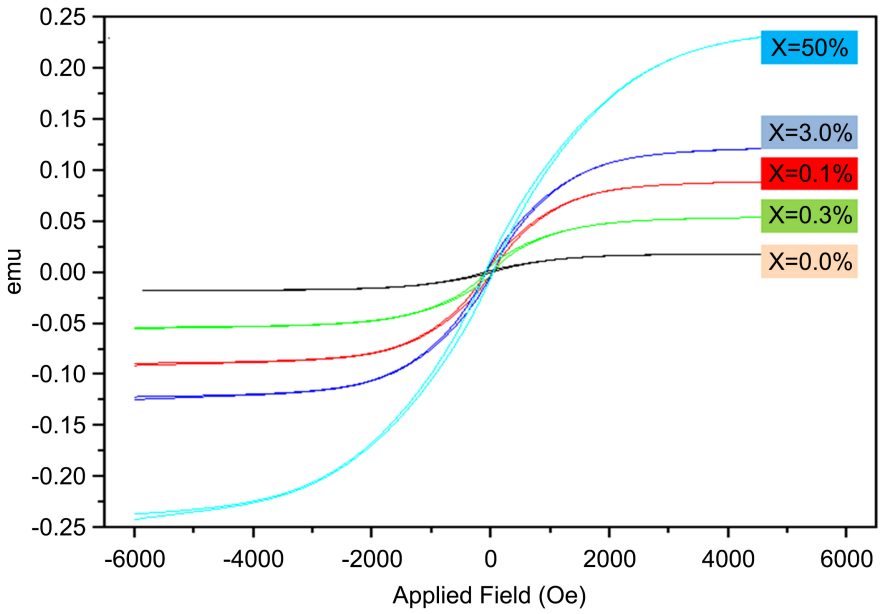

Figure 5. Room temperature hysteresis loops of the as-synthesized nanocomposites.

Table 2. Magnetic parameters of pure, and co-doped $NiO/Ni(OH)_2$.

Sample	M_s (emu/g)	H_c (G)	M_r (emu/g)	SQR (M_r/M_s)	Formula
Pure NiO	0.0183	60.516	0.00105	0.05738	NiO
0.1%mol. Co	0.0906	54.593	0.00514	0.05673	$Co_xNi_{1-x}O/Ni(OH)_2$
0.3%mol. Co	0.0500	65.321	0.00450	0.09000	$Co_xNi_{1-x}O/Ni(OH)_2$
3.0% mol. Co	0.1240	54.887	0.00656	0.05290	$Co_xNi_{1-x}O/Ni(OH)_2$
50% mol. Co	0.240	64.341	0.00903	0.0376	$CoO/NiO/Ni(OH)_2$

The retention (the ability of the nanoparticle to retain magnetization after the applied field is removed) increases with increase in the concentration of Co without respecting the doping fraction trend. This is an indication that another parameter which does not have a direct correlation with crystallite size is responsible for the variation. However, this observation is suggesting that the modification has a link with the surface area of interaction while the surface area is itself linked to the morphology. The highest retention was recorded for the CoO/NiO sample (x = 50%). In a similar manner, the coercivity also varied with particle morphology, while the saturation magnetization increased with increasing concentration of cobalt, then decreased at x = 3.0%, and further increased for x = 50% (CoO/NiO). At the early stages of doping, x < 0.5%, the morphology (porous nano rods) presents a larger surface area of interaction due to porosity and small particle size giving rise to uncompensated spins in the magnetic nanoparticles [32]. At doping fractions of 0.3% < x < 3%, the Co ions, begin to fill the pores instead of replacing the Ni ions and as a consequence reducing the surface area of interaction and the saturation magnetization begins to decrease. At very high doping fractions, X = 50%, there is a complete breakdown of the nano rod microstructure, giving way to a continuous smooth interconnected network of spherical and cubic nano grains, which give rise to the unusual magnetic behavior resulting from the breaking of a large number of exchange bonds.

This also suggests the presence of small magnetic clusters on the surface with lattice imperfections as the translation symmetry of the system is broken down, the antiferromagnetic ordering of NiO becomes disturbed, and the uncompensated spin values increase. The squareness values (remanence ratio) for the as-prepared samples are presented in **Table 1**. The samples have R values in the range 1 > R > 0.5, indicating the existence of exchange coupling in the NPs except CoO/NiO with 0.5 > R, where NPs interact by magnetic interaction [33]. Particle sizes of 7.0 - 7.8 nm are far below the critical particle size of 20.0 nm [34]. The small particle sizes give rise to a high surface area, which are further favored by the morphology of the microstructure which encourages ferromagnetic behavior at room temperature due to a higher concentration of unpaired spins on the surface. The NPs in the samples form single domains with the spins aligned in the same direction, leading to uniform magnetization of the sampled material. The

relatively large coercivity is attributed to the absence of domain walls, and this situation allows the NPs to freely reverse spin by rotation.

4. Conclusion

The magnetic properties manifested by the as-synthesized nanocomposites are known to improve the magnetic memory and hardness of the magnetic materials. Therefore, we can conclude that the Cobalt-doped Nickel Oxide/nickel hydroxide ($Co_xNi_{1-x}O/Ni(OH)_2$) Nano composites synthesized for the very first time by a modified oxalate route using Carambola fruit juice as a precipitating agent, have potential applications in Magnetic memories and hardness of magnetic materials.

Data Availability

All dataset generated to support the conclusions of the study have been completely exploited and are available within the text in the form of Tables, Figures (graphs or photos) for the readers appreciation.

Ethical Approval

This article does not contain any studies with human participants or animals performed.

Authors Contributions

All authors have participated sufficiently in all the phases of the work and agree to take public responsibility for the content, including participation in the concept, design, analysis, writing and/or revision of the manuscript.

Conflicts of Interest

This manuscript is not under consideration in any other journal and the authors declare no conflict of interest.

References

[1] Kim, S., Jeong, J.-E., Hong, J., Lee, K., Lee, M.J., Woo, H.Y. and Hwang, I. (2020) Improved Interfacial Crystallization by Synergic Effects of Precursor Solution Stoichiometry and Conjugated Polyelectrolyte Interlayer for High Open-Circuit Voltage of Perovskite Photovoltaic Diodes. *ACS Applied Materials & Interfaces*, **12**, 12328-12336. https://doi.org/10.1021/acsami.9b22283

[2] Zhang, J., Wang, J., Fu, Y., Zhang, B. and Xie, Z. (2014) Efficient and Stable Polymer Solar Cells with Annealing-Free Solution-Processible NiO Nanoparticles as Anode Buffer Layers. *Journal of Materials Chemistry C*, **2**, 8295-8302. https://doi.org/10.1039/C4TC01302F

[3] Fominykh, K., Tok, G.C., Zeller, P., Hajiyani, H., Miller, T., Döblinger, M., Pentcheva, R., Bein, T. and Fattakhova-Rohlfing, D. (2017) Rock Salt Ni/Co Oxides with Unusual Nanoscale-Stabilized Composition as Water Splitting Electrocatalysts. *Advanced Functional Materials*, **27**, Article ID: 1605121. https://doi.org/10.1002/adfm.201605121

[4] Ren, X., Xie, L., Kim, W.B., Lee, D.G., Jung, H.S. and Liu, S. (2019) Chemical Bath Deposition of Co-Doped TiO_2 Electron Transport Layer for Hysteresis-Suppressed High-Efficiency Planar Perovskite Solar Cells. *Solar RRL*, **3**, 1900176. https://doi.org/10.1002/solr.201900176

[5] Hui, X.U., Zeng, M., Li, J. and Tong, X. (2015) Facile Hydrothermal Synthesis of Flower-Like Codoped NiO Hierarchical Nanosheets as Anode Materials for Lithium-ion Batteries. *RSC Advances*, **5**, 91493-91499. https://doi.org/10.1039/C5RA17017F

[6] Fomekong, R.L. and Saruhan, B. (2021) Titanium Based Materials for High-Temperature Gas Sensor in Harsh Environment Application. *Chemistry Proceedings*, **5**, Article 66. https://doi.org/10.3390/CSAC2021-10480

[7] Chen, P.-C., Hsieh, S.-J., Zou, J. and Chen, C.-C. (2014) Selectively Dealloyed Ti/TiO2 Network Nanostructures for Supercapacitor Application. *Materials Letters*, **133**, 175-178. https://doi.org/10.1016/j.matlet.2014.06.165

[8] Mohamed, M.A., Galwey, A.K. and Halawy, S.A. (2005) A Comparative Study of the Thermal Reactivities of Some Transition Metal Oxalates in Selected Atmospheres. *Thermochimica Acta*, **429**, 57-72. https://doi.org/10.1016/j.tca.2004.08.021

[9] Borel, N.N.M., Foba-Tendo, J., Yufanyi, D.M., Etape, E.P., Eko, J.N. and Ngolui, L.J. (2014) *Averrhoa carambola*: A Renewable Source of Oxalic Acid for the Facile and Green Synthesis of Divalent Metal (Fe, Co, Ni, Zn, and Cu) Oxalates and Oxide Nanoparticles. *Journal of Applied Chemistry*, **2014**, Article ID: 767695. https://doi.org/10.1016/j.tca.2004.08.021

[10] Yong, W.J. (1989) The Thermal Decomposition of Nickel Oxalates Doped with Traces of Other Metal Ions. *Thermochimica Acta*, **147**, 251-260. https://doi.org/10.1016/0040-6031(89)85180-9

[11] Wiedemann, V.H.G. and Nehring, D. (1960) Thermogravimetrische Untersuchungen, III. Der Thermische Zerfall von Nickel- und Magnesiumoxalat und von Nickel-Magnesium-Mischoxalaten in Verschiedenen Gasatmosphären. *Zeitschrift für anorganische und allgemeine Chemie*, **304**, 137-146. https://doi.org/10.1002/zaac.19603040303

[12] Dollimore, D., Griffiths, D.L. and Nicholson, D. (1963) The Thermal Decomposition of Oxalates. Part II. Thermogravimetric Analysis of Various Oxalates in Air and in Nitrogen. *Journal of the Chemical Society*, 2617-2623. https://doi.org/10.1039/jr9630002617

[13] Broadbent, D., Dollimore, D. and Dollimore, J. (1966) The Thermal Decomposition of Oxalates. Part V. The Thermal Decomposition of Nickel Oxalate Dihydrate. *Journal of the Chemical Society*, 278-281. https://doi.org/10.1039/j19660000278

[14] Kyung, H.K., Sho, F. and Yoshio, A. (2022) Incorporation of Co^{2+}, Cu^{2+} and Zn^{2+} Ions into Nickel Oxide Thin Films and Their Enhanced Electrochemical and Electrochromic Performances. *International Journal of Electrochemical Science*, **17**, Article ID: 220125. https://doi.org/10.20964/2022.01.39

[15] Akkaya, M. and Akman, E. (2021) The Synthesis Copper-Doped Nickel Oxide and Application of Hybrid Nanolubricants as a Compressor Oil. *Gazi Mühendislik Bilimleri Dergisi*, **7**, 134-142. https://doi.org/10.30855/gmbd.2021.02.06

[16] Kate, R.S. and Deokate, R.J. (2020) Effect of Cobalt Doping on Electrochemical Properties of Sprayed Nickel Oxide Thin Films. *Materials Science for Energy Technologies*, **3**, 830-839. https://doi.org/10.1016/j.mset.2020.06.008

[17] Cuong, N.D., Tran, T.D., Nguyen, Q.T., Van Minh, H.H., Hoa, T.T., Quang, D.T., Klysubun, W. and Tran, P.D. (2021) Highly Porous Codoped NiO Nanorods: Facile

Hydrothermal Synthesis and Electrocatalytic Oxygen Evolution Properties. *Royal Society Open Science*, **8**, Article ID: 202352. https://doi.org/10.1098/rsos.202352

[18] Marand, Z.R., Kermanpur, A., Karimzadeh, F., Barea, E.M., Hassanabadi, E., Anaraki, E.H., Julián-López, B., Masi, S. and Mora-Seró, I. (2020) Structural and Electrical Investigation of Cobalt-Doped NiO_x/Perovskite Interface for Efficient Inverted Solar Cells. *Nanomaterials*, **10**, Article 872. https://doi.org/10.3390/nano10050872

[19] Sharma, J., Srivastava, P., Singh, G., Akhtar, M.S. and Ameen, S. (2015) Biosynthesized NiO Nanoparticles: Potential Catalyst for Ammonium Perchlorate and Composite Solid Propellants *Ceramics International*, **41**, 1573-1578. https://doi.org/10.1016/j.ceramint.2014.09.093

[20] Etape, E.P., Ngolui, L.J., Foba-Tendo, J., Yufanyi, D.M. and Namondo, B.V. (2017) Synthesis and Characterization of Cook, TiO_2 and CuO-TiO_2 Mixed Oxide by a Modified Oxalate Route. *Journal of Applied Chemistry*, **2017**, Article ID: 4518654. https://doi.org/10.1155/2017/4518654

[21] Mansour, S.A.A. (1993) Spectroscopic and Microscopic Investigations of the Thermal Decomposition Course of Nickel Oxysalts. Part 3. Nickel Oxalate Dihydrate. *Thermochimica Acta*, **230**, 243-257. https://doi.org/10.1016/0040-6031(93)80364-G

[22] Yu, C., Zhang, L., Shi, J., Zhao, J., Gao, J. and Yan, D. (2008) A Simple Template-Free Strategy to Synthesize Nanoporous Manganese and Nickel Oxides with Narrow Pore Size Distribution and Their Electrochemical Properties. *Advanced Functional Materials*, **18**, 1544-1554. https://doi.org/10.1002/adfm.200701052

[23] Małecka, B., Małecki, A., Drożdż-Cieśla, E., Tortet, L., Llewellyn, P. and Rouquerol, F. (2007) Some Aspects of Thermal Decomposition of $NiC_2O_4{\cdot}2H_2O$. *Thermochimica Acta*, **466**, 57-62. https://doi.org/10.1016/j.tca.2007.10.010

[24] Boyle, B.J., King, E.G. and Conway, K.C. (1954) Heat of formation of Nickel Oxide and Cobalt Oxide (NiO and CoO) of Cobustion Calorimetry. *Journal of the American Chemical Society*, **76**, 3835-3837. https://doi.org/10.1021/ja01643a072

[25] Lenin, R. and Joy, P.A. (2016) Role of Primary and Secondary Surfactant Layers on the Thermal Conductivity of Lauric Acid Coated Magnetite Nanofluids. *The Journal of Physical Chemistry C*, **120**, 11640-11651. https://doi.org/10.1021/acs.jpcc.5b12476

[26] Lin, Z., *et al.* (2016) Morphology-Controllable Synthesis and Thermal Decomposition of Ag and Ni oxalate for Ag-Ni Alloy Electrical Contact Materials. *Materials & Design*, **108**, 640-647. https://doi.org/10.1016/j.matdes.2016.06.123

[27] Etape, E.P., Foba-Tendo, J., Namondo, B.V., Yufanyi, D.M., Tedjieukeng, H.M.K., Fomekonga, R.L. and Ngolui, L.J. (2020) Nano Size $CaCu_3Ti_4O_{12}$ Green Synthesis and Characterization of a Precursor Oxalate Obtained from *Averrhoa carambola* Fruit Juice and Its Thermal Decomposition to the Perovskite. *Journal of Nanomaterials*, **2020**, Article ID: 8830136. https://doi.org/10.1155/2020/8830136

[28] Liu, F., Yang, X., Qiao, Z., Zhang, L., Cao, B. and Duan, G. (2017) Highly Transparent 3D NiO-Ni/Ag-Nanowires/FTO Micro-Supercapacitor Electrodes for Fully Transparent Electronic Device Purpose. *Electrochimica Acta*, **260**, 281-289. https://doi.org/10.1016/j.electacta.2017.11.011

[29] Govindarajan, B., Palanimuthu, R. and Manikandan, K.M. (2019) Influence of Mg Doping in Magnetic Properties of NiO Nanoparticles and Its Electrical Applications. *Journal of Materials Science: Materials in Electronics*, **30**, 6519-6527.

[30] Wardani, M., Yulizar, Y., Abdullah, I. and Apriandanu, D.O.B. (2019) Synthesis of NiO Nanoparticles via Green Route Using *Ageratum conyzoides* L. Leaf Extract and

Their Catalytic Activity. *Proceedings of* 13*th Joint Conference on Chemistry* (13*th JCC*), Semarang, 7-8 September 2018, Article ID: 012077. https://doi.org/10.1088/1757-899X/509/1/012077

[31] Anand, G.T., Nithiyavathi, R., Ramesh, R., Sundaram, S.J. and Kaviyarasu, K. (2020) Structural and Optical Properties of Nickel Oxide Nanoparticle. *Surfaces and Interfaces*, **18**, Article ID: 100460.

[32] Stoner, E.C. and Wohlfarth, E.P. (1948) A Mechanism of Magnetic Hysteresis in Heterogeneous Alloys. *Philosophical Transactions of the Royal Society A*, **240**, 599-642. https://doi.org/10.1098/rsta.1948.0007

[33] Etape, E.P., Foba-Tendo, J., Ngolui, L.J., Namondo, B.V., Yollande, F.C. and Nguimezong, M.B.N. (2018) Structural Characterization and Magnetic Properties of Undoped and Ti-Doped ZnO Nanoparticles Prepared by Modified Oxalate Route. *Journal of Nanomaterials*, **2018**, Article ID: 9072325. https://doi.org/10.1155/2018/9072325

[34] Mahmed, N., Heczko, O., Söderberg, O. and Hannula, S.P. (2011) Room Temperature Synthesis of Magnetite ($Fe_{3-\delta}O_4$) Nanoparticles by a Simple Reverse Co-Precipitation Method. *IOP Conference Series*: *Materials Science and Engineering*, **18**, Article ID: 032020. https://doi.org/10.1088/1757-899X/18/3/032020